

Check for updates

Dynamic Electron Spring Effect in Hollow Fe₂O₃/CoSe₂ Heterostructure Enhance Ethanol Electro-Oxidation Activity and Stability

Shunlian Ning, Yongqi Jian, Guang-Qiang Yu, Jinchang Xu, Ming-Hsien Lee, Dawei Wang, HongYan Chen, Mihail Barboiu, Xiaojun Liu, Dengke Zhao,* Linjing Yang,* and Nan Wang*

Developing efficient non-noble electrocatalysts with high activity and selectivity for ethanol oxidation reaction (EOR) across a wide potential range remains a significant challenge in hybrid energy systems. Herein, hollow Fe₂O₃/CoSe₂ heterostructures (H-Fe₂O₃/CoSe₂@C) via interface engineering are reported as highly effective EOR promising electrocatalysts. Characterizations reveal that Fe₂O₃ functions as a dynamic electron spring to tune the electronic structure of Co sites, accelerating the formation of the Fe₂O₃/CoOOH heterostructure while suppressing Fe₂O₃/CoO₂ evolution. In situ Raman spectroscopy and theoretical calculation confirm that the Fe₂O_{3/}CoOOH heterostructure enhances EOR kinetics and lowers the energy barrier of the potentialdetermining step. Quasi in situ X-ray photoelectron spectroscopy further demonstrates that Fe₂O₃ stabilizes Co³⁺against overoxidation, expanding the operational potential window. Consequently, H-Fe₂O₃/CoSe₂@C achieves outstanding EOR performance, exhibiting 10 mA cm⁻² @1.30 V vs. RHE with a high faradaic efficiency of 99% at 1.30 V. Ethanol-assisted Zn-Air battery/water splitting devices based on H-Fe₂O₃/CoSe₂@C demonstrate enhanced energy conversion efficiency, with voltage reduced by 210 and 180 mV at 10 mA cm⁻², respectively. This work provides critical insights for designing heterostructure electrocatalysts and advancing the utilization of biomass energy.

1. Introduction

The advancement of water electrolysis (WE) and rechargeable Zn-air batteries (r-ZABs) is paramount in addressing the global challenges of energy scarcity and environmental degradation. Nevertheless, the sluggish kinetics and the high thermodynamic potential (1.23 V vs. RHE) of oxygen evolution reaction (OER) significantly hinder the reduction of anode energy consumption and the improvement of cycling life in these systems.[1-3] Despite the extensive research on advanced OER electrocatalysts, the intrinsically low activity and severe reconstruction of these materials under high potential conditions result in substantial energy losses and shortened lifespan. In contrast, ethanol oxidation reaction (EOR) exhibits more favorable kinetics and lower thermodynamic potential, which makes it a promising alternative to OER for constructing ethanol-assisted WE and ZABs. By replacing OER with EOR, it is possible

S. Ning, D. Wang, H. Chen
MOE Laboratory of Bioinorganic and Synthetic Chemistry
GBRCE for Functional Molecular Engineering
Lehn Institute of Functional Materials, IGCME
School of Chemistry
Sun Yat-Sen University
Guangzhou, Guangdong 510275, China
Y. Jian, G.-Q. Yu, N. Wang
Siyuan laboratory
Guangzhou Key Laboratory of Vacuum Coating Technologies and New
Energy Materials
Guangdong Provincial Engineering Technology Research Center of
Vacuum Coating Technologies and New Energy Materials
Guangdong Provincial Key Laboratory of Nanophotonic Manipulation
Department of Physics Jinan University Guangzhou

Guangdong 510632, China E-mail: nanwang@email.jnu.edu.cn

The ORCID identification number(s) for the author(s) of this article can be found under https://doi.org/10.1002/adfm.202509007

DOI: 10.1002/adfm.202509007

J. Xu Guangdong Provincial Key Laboratory of Terahertz Quantum Electromagnetics GBA Branch of Aerospace Information Research Institute Chinese Academy of Sciences Guangzhou 510700, China M.-H. Lee Department of Physics Tamkang University New Taipei 25137, Taiwan M. Barboiu Institut Europeen des Membranes Adaptive Supramolecular Nanosystems Group University of Montpellier **ENSCM-CNRS** UMR5635 Place E. Bataillon CC047, Montpellier 34095, France Department of Mechanical Engineering Oakland University Rochester Hills, Michigan 48309, United States

www.afm-journal.de

16163028, Downloaded from https://advanced.onlinelibrary.wiley.com/ai/10.1002/adfm.20209007 by National Taiwan University, Wiley Online Library on [27/102025]. See the Terms and Conditions (https://onlinelibrary.wiley.com/terms-and-conditions) on Wiley Online Library for rules of use; OA articles are governed by the applicable Creative Commons License

to significantly reduce the energy input required for anode oxidation and improve system stability. Building upon this concept, we previously introduced a unique "zinc-ethanol-air battery" that utilizes a non-noble metal catalyst. This innovative design achieved a reduction in charging voltage compared to traditional zinc-air batteries, demonstrating significant efficiency improvements. Furthermore, EOR can produce acetic acid ester and acetate salt, which find extensive applications in diverse sectors including the food, pharmaceutical, and fine chemical industries. 10,11 However, the EOR process involves multiple electron transfers, necessitating the development of cost-effective electrocatalysts to enhance both activity and selectivity.

Transition metal selenides, such as CoSe2, have ideal candidates as electrocatalysts for EOR due to their metallic properties and excellent oxophilicity.[12] Our recent research has shown that CoSe₂ can function as a pre-catalyst, undergoing reconstruction to form Co3+OOH, and exhibit high EOR activity by precisely modulates the electron spin state through coordination structure changes.[13] However, the susceptibility of Co3+OOH to further oxidation to Co4+O2 under high potentials, leads to increased competition from OER and a consequent reduction in faradaic efficiency (FE) and EOR stability.[14] To overcome the challenge, interface engineering has been proposed as a potential strategy,^[15] the formation of a built-in electric field at interface can optimize the electronic structure and spin state of active sites, stabilize their valence state, and ultimately enhance the activity and selectivity of electrocatalysts. [16-18] Nevertheless, maintaining the stable valence state of the active site at the interface under dynamic conditions, particularly in the context of high oxidation potential, represents a significant challenge. But it is crucial for extending the potential window and selectivity of CoSe, electrocatalysts toward EOR. So, it is essential to explore the potential of CoSe₂-based heterojunctions for achieving high EOR activity and selectivity across a wide range of reaction potentials. Furthermore, additional research is required to elucidate the mechanism of catalytic activity enhancement, thereby providing guidance for the subsequent design of more efficient EOR electrocatalysts.

In addition to the intrinsic activity, the physical structure of an electrocatalyst is equally crucial for catalytic performance. Hollow nanomaterials with high surface-to-volume ratios are regarded as ideal nanoreactors in various electrocatalysis, which can increase accessible active sites and accelerate charge/mass transfer in the reaction. $^{[1,19-25]}$ Therefore, reasonably constructing CoSe_2 heterojunction with a hollow structure is expected further improve the electroactivity and selectivity of EOR.

Inspired by these principles, we developed a novel ion exchange-etching-selenization strategy to synthesize hollow carbon supported Fe₂O₃/CoSe₂ heterostructures (H-

D. Zhao School of Materials Science and Engineering Henan Normal University

Xinxiang 453007, China E-mail: zhaodengke@htu.edu.cn

L. Yang

Faculty of Metallurgical and Energy Engineering Kunming University of Science and Technology

Kunming 650093, China

E-mail: eslinjingyang@kust.edu.cn

 $Fe_2O_3/CoSe_2@C)$ as highly efficient EOR electrocatalysts. In situ characterization and electrochemical analysis confirm that Fe_2O_3 dynamically stabilizes the Co valence state of during EOR, promoting the Co^{2+} to Co^{3+} transition at a lower voltage and delaying the over-oxidation to Co^{4+} at a higher voltage, which we term the 'dynamic electron spring effect'.

In situ FTIR spectroscopy and ^{1H}NMR analysis validate a fourelectron transfer EOR mechanism, while density functional theory (DFT) calculations identify the Co site as the primary active site. The Fe₂O₃ component reduces the energy barrier of the potential-determining step (PDS), thereby improving the EOR kinetics and electroactivity. The spin-electronic analysis further reveals that Fe₂O₃ regulates the spin state of Co sites to increase the electron filing of dz² and dyz orbitals, which can weaken the adsorption capacity of intermediates during the EOR process, thereby promoting the transfer of intermediates to enhance EOR kinetics and electroactivity. Therefore, H-Fe₂O₃/CoSe₂@C demonstrates enhanced EOR electroactivity (1.30 V vs. RHE at 10 mA cm⁻²), excellent stability (100 h at 10 mA cm⁻²), and high FE of acetate (over 90% at potential from 1.30 to 1.70 V vs. RHE). The cell voltages in hybrid WE and ZAB are significantly reduced by 210 and 180 mV at 10 mA cm⁻², respectively.

2. Results and Discussion

The active sites responsible for EOR in Co-based catalysts are predominantly attributed to Co³+ species, which accords with the mechanism of nucleophilic oxidation reaction. [26,27] For a more detailed overview, please refer to Figure S1 (Supporting Information). In accordance with Pourbaix diagrams generated from 'materials project.org, [28–30] the Co²+ is oxidized to Co³+ (CoOOH) at 0.95 V and further to Co⁴+ (CoO₂) at 1.37 V_{RHE} under pH 14 conditions (Figure S2, Supporting Information), while the CoO₂ species are regarded as main OER active sites. These transformations indicate that Co³+ only exists within a narrow potential window of 0.95 to 1.37 V_{RHE}. The limited stability range of Co³+ leads to significant competition between EOR and oxygen evolution reaction (OER), which can hinder the efficient application of EOR.

Interestingly, as illustrated in Figure 1a, one can find that Fe_2O_3 remains stable between +0.13 and +1.61 V_{RHE} , which maybe can act as an 'electron spring' to dynamically stabilize the valence state of Co sites, and significantly extend the EOR potential window of CoSe2. This 'spring effect' operates through a dual mechanism: first, Fe₂O₃, with its strong oxidizing nature, interacts with CoSe₂, which exhibits high electronegativity, thus resulting in electron transfer from CoSe₂ to Fe₂O₃ in the low potential regions, which can lead to Cosites in CoSe2 becoming more electron-deficient and transforming into $Co^{(2+\delta)^+}$ to facilitate reconstruction of CoSe2 to form CoOOH at lower potential. This represents the "push" aspect of the spring effect. Second, Fe₂O₃ is oxidized to FeO₄²⁻ at \approx +1.61 V vs. RHE, meaning electrons transfer from Fe₂O₃ to the external circuit or nearby atoms. Consequently, neighboring Co⁴⁺ can accept some of these electrons, reducing to $Co^{(4-\delta)^+}$. This illustrates the "pull" aspect, which can pull Co⁴⁺ to lower oxidation states at higher potentials.

In summary, Fe₂O₃ exerts a dynamic 'spring effect' on cobalt, maintaining the valence state of cobalt sites around Co³⁺. By pushing Co²⁺ to higher oxidation states at low potentials and

16163028. 0, Downloaded from https://advanced.onlinelibrary.wiley.com/doi/10.1002/adfm.202509007 by National Taiwan University. Wiley Online Library on [27/10/2025]. See the Terms

and-conditions) on Wiley Online Library for rules of use; OA articles are governed by the applicable Creative Commons

www.afm-journal.de

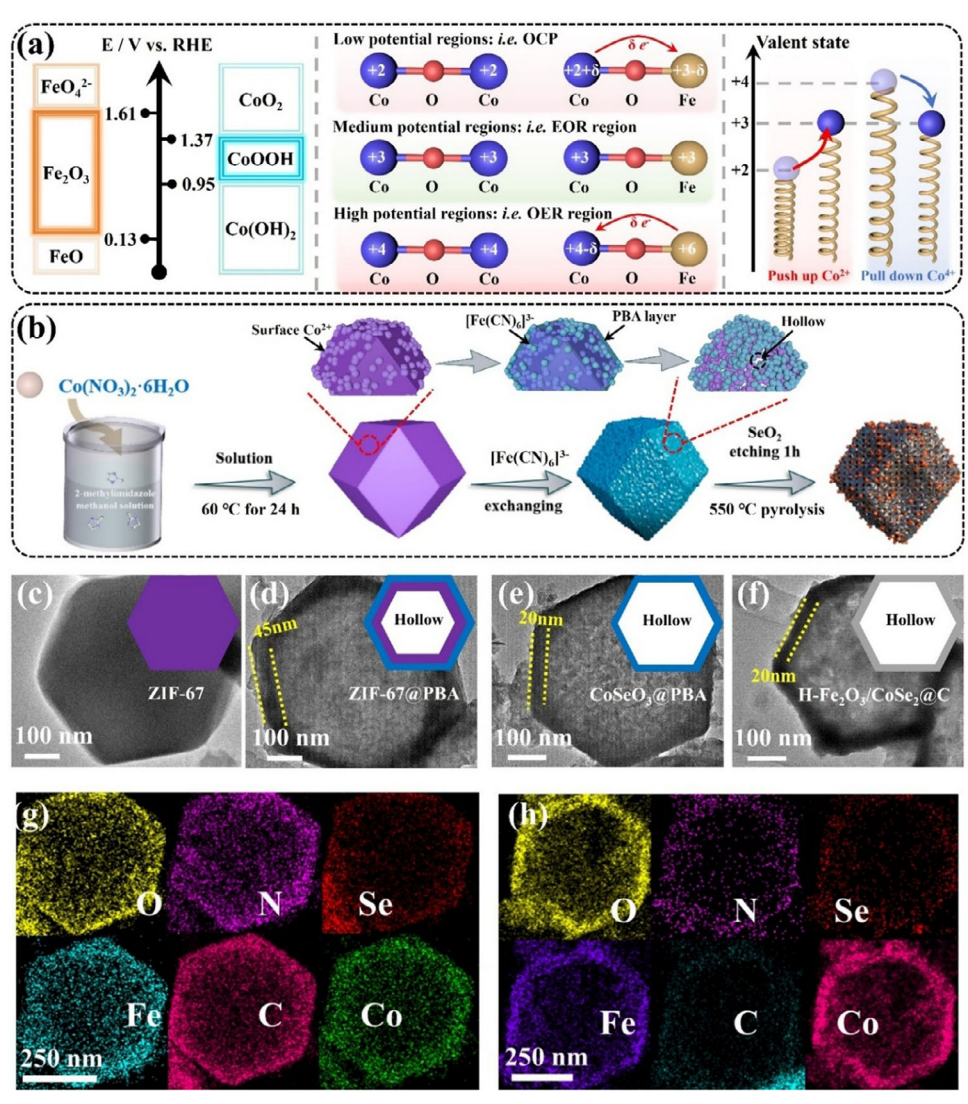


Figure 1. a) The schematic diagram of the working principle of Fe_2O_3 (spring'. b) Scheme for showing the synthesis process of H- Fe_2O_3 /CoSe₂@C. c–f) TEM images of different samples. g,h) EDS mapping images of CoSeO₃@PBA and H- Fe_2O_3 /CoSe₂@C.

pulling Co^{4+} to lower oxidation states at high potentials, Fe_2O_3 effectively stabilizes Co^{3+} over a broader potential range. This stabilization mitigates competition between EOR and OER, enhancing the practical application of cobalt-based catalysts in electrochemical reactions.

To validate this concept, Fe₂O₃/CoSe₂ heterojunctions were synthesized as depicted in Figure 1b. The process begins with the synthesis of ZIF-67 through self-assembly between Co(NO)₃ and 2-MIM. Subsequently, ZIF-67@PBA is obtained by anion exchange between K₃[Fe(CN)₆] and 2-MIM. [31,32] Following this, SeO₂ solution is added to etch ZIF-67@PBA, forming SeO₃@PBA through reactions such as SeO₂ + H₂O \rightarrow 2H⁺ + SeO₃²⁻ and Co²⁺ + SeO₃²⁻ \rightarrow CoSeO₃@PBA. Finally, H-Fe₂O₃/CoSe₂@C is obtained by annealing of SeO₃@PBA under N₂ atmosphere. XRD patterns (Figure S3a, Supporting Information) confirm the transitions of the crystal phase during the synthesis process. The distinct diffraction peaks of ZIF-67 are observed in the absence of K₃[Fe(CN)₆] and SeO₃ solutions. The

addition of K₃[Fe(CN)₆] results in the attenuation of the ZIF-67 peaks and the appearance of PBA peaks. [33] indicating the transformation of ZIF-67 to PBA. Upon further addition of SeO2 solution, the ZIF-67 peaks of disappear, suggesting that the residual ZIF-67 is fully etched by acid solution. At an annealing temperature is 400 °C, a portion of the PBA phase remains, and the formation of CoSe₂ phases is observed (Figure S3b, Supporting Information). After annealing at 500 °C, the PBA phase is no longer detectable, and new diffraction peaks corresponding to (211) and (222) plane of Fe₂O₃ emerge (Figure S3c, Supporting Information), indicating complete conversion to Fe₂O₃ and CoSe₂. Raman spectrum (Figure S4, Supporting Information) further verifies these results, with characteristic peaks for CoSe₂ $(A_g \text{ at } 184 \text{ cm}^{-1}, E_g \text{ at } 480 \text{ cm}^{-1}, A_{1g} \text{ at } 690 \text{ cm}^{-1})$, [34] and Fe_2O_3 (324, 392 and 546 cm⁻¹).[35] As a reference, CoSe₂@C was also prepared through the same protocol without adding K₂[Fe(CN)₆], with the XRD pattern shown in Figure S5 (Supporting Information).

16163028.0, Downloaded from https://advanced.onlinelibrary.wiley.com/doi/10.1002/adfm.20209007 by National Tawan University, Wiley Online Library on [27/10/2025]. See the Terms and Conditional Tawan University, Wiley Online Library on [27/10/2025]. See the Terms and Conditional Tawan University, Wiley Online Library on [27/10/2025]. See the Terms and Conditional Tawan University, Wiley Online Library on [27/10/2025]. See the Terms and Conditional Tawan University, Wiley Online Library on [27/10/2025]. See the Terms and Conditional Tawan University.

conditions) on Wiley Online Library for rules of use; OA articles are governed by the applicable Creative Commons

www.afm-journal.de

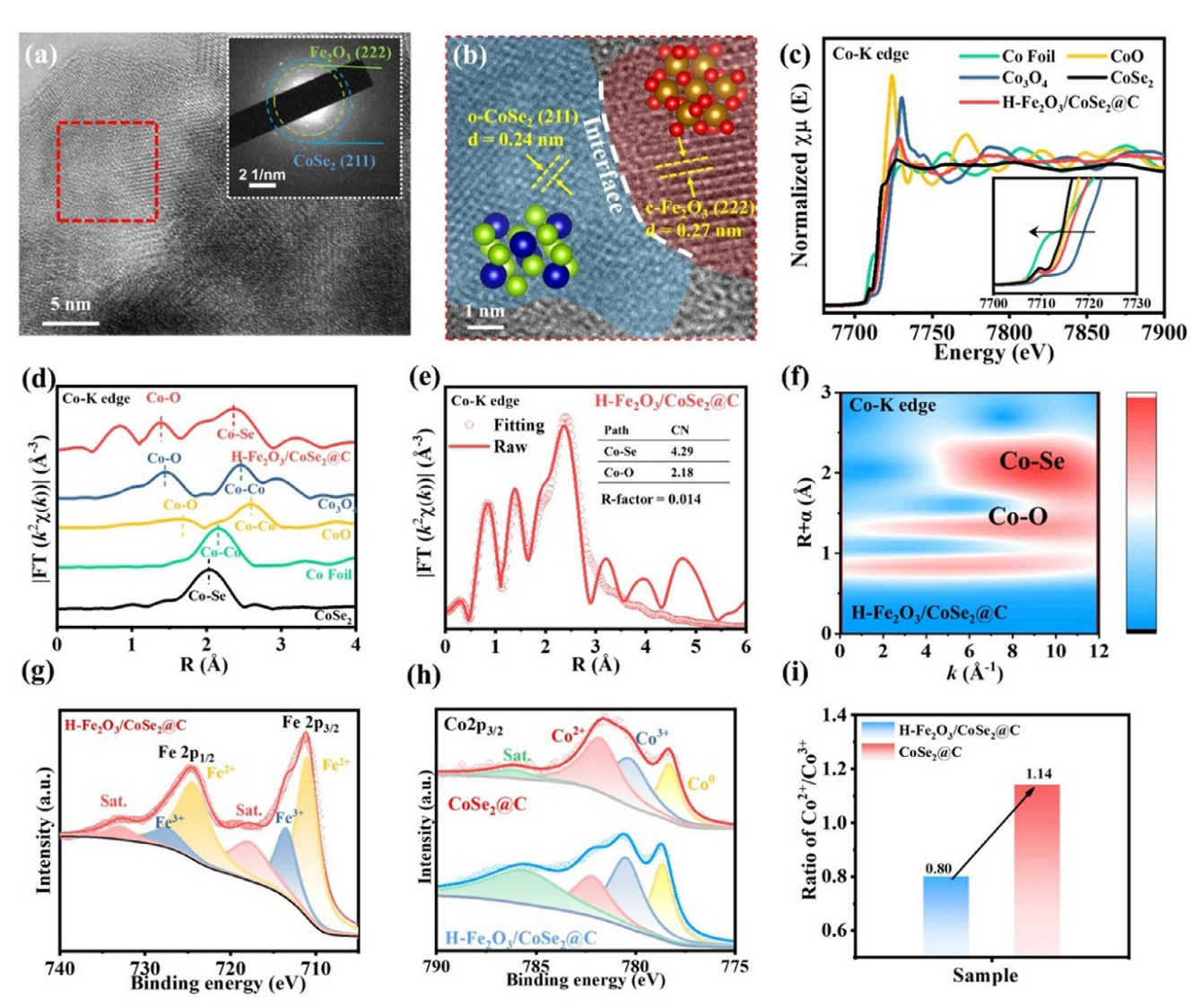


Figure 2. a,b) HRTEM images of H-Fe₂O₃/CoSe₂@C. (Inset: corresponding SAED pattern). c) The Co K edge XANES spectra of H-Fe₂O₃/CoSe₂@C, Co Foil, Co₃O₄, CoSe₂ and CoO. d) The corresponding FT-EXAFS spectra of the Co K edge. e) First-shell fitting of the FT-EXAFS spectrum of H-Fe₂O₃/CoSe₂@C. f) The WT-EXAFS of H-Fe₂O₃/CoSe₂@C. g) The XPS spectra of Fe₂P. h) The XPS spectra of Co₂P. i) The relative ratio of Co²⁺/Co³⁺ according to the XPS results.

As observed in SEM images (Figure S6, Supporting Information), ZIF-67 presents a regular dodecahedral structure, which is retained in SeO₃@PBA, albeit with the presence of NPs on the surface. Additionally, H-Fe₂O₃/CoSe₂@C maintains the dodecahedron morphology (Figure S7, Supporting Information). As illustrated in TEM images (Figure 1c-f), ZIF-67 presents a solid structure. However, upon interaction with PBA, the structure transforms into a hollow structure with a wall thickness of 45 nm, which is further reduced to 20 nm after SeO₃ etching. Following annealing, H-Fe₂O₃/CoSe₂@C remains this hollow structure with the same thicknesses. EDS mapping (Figure 1g,h) indicates that the elements C, N, O, Co, Fe, and Se are predominantly distributed on the surface of SeO₃@PBA and H-Fe₂O₃/CoSe₂@C. The corresponding element contents in H-Fe₂O₃/CoSe₂@C, as determined by EDS (Figure S8, Supporting Information), are 20.74, 4.44, 10.92, 29.14, 25.43, and 9.33 wt.%,

respectively. Given that EDS is a surface testing technique, we further precisely determined the contents of Fe and Co in the sample by means of ICP-OES, and the corresponding contents were 13.48 and 32.12. wt.%, respectively (Table \$1, Supporting Information). The Fe content is lower than the EDS results, which indicates that Fe species is mainly concentrated on the surface. (Table S1, Supporting Information). The distinctive hollow structure of H-Fe₂O₃/CoSe₂@C provides a high specific surface area (49.6 m² g⁻¹) and a well-developed pore structure with a multitude of micro- and mesopores (Figure S9, Supporting Information), which can facilitate the exposure of a greater number of active sites and enhance charge and mass transfer during the electrochemical reactions.[36] The crystalline phases were further analyzed by HRTEM images. As depicted in Figure 2a, distinct diffraction rings and lattice fringes corresponding to the Fe₂O₃ (222) plane and the CoSe₂ (211) plane can be clearly observed.

www.advancedsciencenews.com



www.afm-journal.de

16163028, 0, Downloaded from https://advanced.onlinelibrary.wiley.com/doi/10.1002/adfm.202509007 by National Taiwan University, Wiley Online Library on [27/10/2025]. See the Terms and Conditions (https://onlinelibrary.wiley.com/terms

-and-conditions) on Wiley Online Library for rules of use; OA articles are governed by the applicable Creative Commons

Additionally, discernible interfaces between each phase, indicated by a white line, confirm the formation of the Fe₂O₃/CoSe₂ heterojunction (Figure 2b).

X-ray absorption spectroscopy (XAS) is employed to gain further insight into the chemical states and coordination environment of the Co site in H-Fe₂O₃/CoSe₂@C. As shown in Figure 2c, the X-ray absorption near edge structure (XANES) spectra (Figure 2c) reveal that the absorption edge energy for Co sites in H-Fe₂O₃/CoSe₂@C lies between those of CoO and Co₃O₄, suggesting that the valence state of Co is between +2 and +3. Further investigation into local coordination structure was conducted through the Fourier transform (FT) k^2 -weighted extended X-ray absorption fine structure (EXAFS) spectra (Figure 2d). The analysis identifies two distinct coordination environments for the Co sites, corresponding to Co-Se (2.4 Å)[37] and Co-O bonds (1.4 Å).[38] The presence of Co-O bonds implies that Fe₂O₃/CoSe₂ phases may be interconnected by Co–O–Fe bond. To further analyze the coordination numbers (CN) of Co sites, the EXAFS spectra were fitted. Detailed fitting results are provided in Figure 2e, Figure S10, and Table S2 (Supporting Information), showing the CN of Co sites in as-made samples is 6 (with 4 Se atoms and 2 O atoms), closely matching theoretical value, further confirming the formation of orthorhombic CoSe₂. The corresponding wavelet transforms (WT) (Figure 2f; Figure S11, Supporting Information) further support these findings. The Co foil exhibits a strong signal at 5.5 Å⁻¹, which is attributed to Co—Co bond. In contrast, the CoO and Co₃O₄ display two regions of enhanced intensity, corresponding to the Co-O and Co-Co bonds, respectively. Similarly, the H-Fe₂O₃/CoSe₂@C sample exhibits intensity maxima attributed to the Co-Se (9.0 Å⁻¹) and Co-O (6.3 Å^{-1}) bonds.

XPS tests were performed to further examine the oxidation state of synthesized samples. In Figure S12a (Supporting Information), the full XPS survey of H-Fe₂O₃/CoSe₂@C exhibits clear characteristic peaks of N1s, O1s, C1s, Se3d, Fe2p and Co2p, consistent with EDS spectra. The Se3d spectrum (Figure S12b, Supporting Information) reveals peaks at binding energies (BE) of 54.6 and 55.1 eV, attributed to $Se3d_{5/2}$ and $Se3d_{3/2}$ respectively. In addition, another pair of peaks at 58.78 and 60.26 eV are assigned to Co3p_{3/2} and Co3p_{1/2}.^[39,40] Moreover, the O1s spectrum (Figure S12c, Supporting Information) shows three deconvoluted peaks, belonging to lattice oxygen (O_1) , defect oxygen (O_D) , and adsorbed hydroxyl groups (OH_{ad}), respectively.^[41,42] In the Fe2p spectrum (Figure 2g), three pair peaks can be observed, corresponding to Fe²⁺, Fe³⁺, and satellite peaks, respectively.^[43] The BEs of Co2p are special (Figure 2h), where the peaks located at 778.6, 780.2, 781.3, and 786.3 eV correspond to Co^0 , Co^{3+} , Co^{2+} , and satellite peaks, respectively.[44] From Figure 2i, compared with the CoSe₂@C, the ratio of Co²⁺/Co³⁺ ratio decreases significantly from 1.14 to 0.80, indicating that the introduction of Fe₂O₃ can regulate the electronic structure of Co site in CoSe₂ to increase the average valence state of Co sites, which is beneficial to enhance the overall performance. [45] The above situation is further analyzed through molecular orbital theory (Figure S13, Supporting Information), where we consider the electronic configurations of Co²⁺ (3d⁷: $t_{2g}^{\ 5}eg^2$) and Fe³⁺ (3d⁵: $t_{2g}^{\ 3}eg^2$) in the heterojunction. In general, the symmetry of the $t_{\rm 2g}$ orbital is easier to form a π -conjugated system with the p orbital. Due to the existence of unpaired electrons in the t_{2g} orbitals of Fe³⁺, which

can weaken the e^--e^- repulsion between the bridging O^{2^-} and Co^{2^+} to trigger partial electron transfer from Co^{2^+} to Fe^{3^+} , thereby prometing the electron transfer at the interface, further confirm the XPS results.

The EOR performance of as-prepared samples was evaluated by LSVs. As shown in Figure 3a, H-Fe₂O₃/CoSe₂@C exhibits superior EOR electroactivity than that of CoSe₂@C and RuO₂, with voltages of only 1.30, 1.41, and 1.52 V vs. RHE at current density of 10, 50 and 100 mA cm⁻², respectively (Figure 3b). These results are comparable to some reported advanced EOR electrocatalysts (Table S3, Supporting Information). In Figure S14a,b (Supporting Information), the OER electroactivity of as-prepared samples was also assessed. Although, H-Fe₂O₃/CoSe₂@C also shows the optimal activity with lower overpotentials of 250 and 300 mV at 10 and 50 mA cm⁻² respectively, the energy loss is still significant compared to EOR (Figure S14c, Supporting Information), in which OER replaced by EOR can substantially reduce reaction potential, such as a potential reduction of 180 mV at 10 mA cm⁻². The Tafel plots for EOR (Figure 3c) show that H-Fe₂O₃/CoSe₂@C has a Tafel slope of only 43 mV dec⁻¹, much lower than the Tafel slope of OER (97 mV dec⁻¹), indicating EOR has more favorable kinetics than OER (Figure S14d, Supporting Information). The result is further supported by EIS data (Figure S15, Supporting Information), where H-Fe₂O₃/CoSe₂@C exhibits a lower R_{ct} for EOR compared to OER. Then, C_{dl} was further analyzed based on the CV curves at different scan rates (Figure S16a,b, Supporting Information), the C_{dl} of H-Fe₂O₃/CoSe₂@C is 31 mF cm⁻², which is higher than that of CoSe₂@C (24 mF cm⁻²) (Figure S16c, Supporting Information), suggesting that the larger ECSA of H-Fe₂O₃/CoSe₂@C. To eliminate the influence of ECSA, the normalized LSV was further analyzed (Figure \$16d, Supporting Information), H-Fe₂O₃/CoSe₂@C still displayed better EOR performance than that of CoSe₂@C, indicating that Fe₂O₃ can improve the intrinsic activity of CoSe₂@C. The EOR stability of H-Fe₂O₃/CoSe₂@C was further examined through a CP test, with the electrolyte being refreshed every 20 h to mitigate the effects of ethanol concentration reduction. As displayed in Figure 3d, H-Fe₂O₃/CoSe₂@C demonstrates excellent long-term EOR stability, and the potential can maintain well within 100 h with only \approx 30 mV of attenuation.

In order to further determine active species for EOR, we conducted an analysis of the EOR electroactivity of the samples after acid treatment. As shown in Figure S17a (Supporting Information), the EOR electroactivity of H-Fe₂O₃/CoSe₂@C occurs a significant attenuation after acid treatment, indicating that the main active originates from Fe₂O₃/CoSe₂. Moreover, we also analyzed the effect of Fe₂O₃ on the electroactivity of as-made samples. In Figure S17b (Supporting Information), it can be observed that the EOR electroactivity of H-Fe₂O₃/CoSe₂@C with different Fe contents, with the increase of the amount of Fe, first increases and then decreases. The result suggests that the outstanding EOR electroactivity is derived from the synergistic interaction between Fe₂O₃ and CoSe₂, and Fe₂O₃ exerts a crucial influence in boosting the EOR activity of CoSe₂.

To identify EOR products, 1H NMR measurements with D_2O as the solvent (Figure S18, Supporting Information) were performed to analyze the products. The characteristic peaks of acetic acid were detected in electrolytes after the CP test, suggesting that ethanol was oxidized to acetate. According to related

16163028. 0, Downloaded from https://advanced.onlinelibrary.wiley.com/doi/10.1002/adfm.202509007 by National Taiwan University, Wiley Online Library on [27/10/2025]. See the Terms and Conditional Co

conditions) on Wiley Online Library for rules of use; OA articles are governed by the applicable Creative Commons

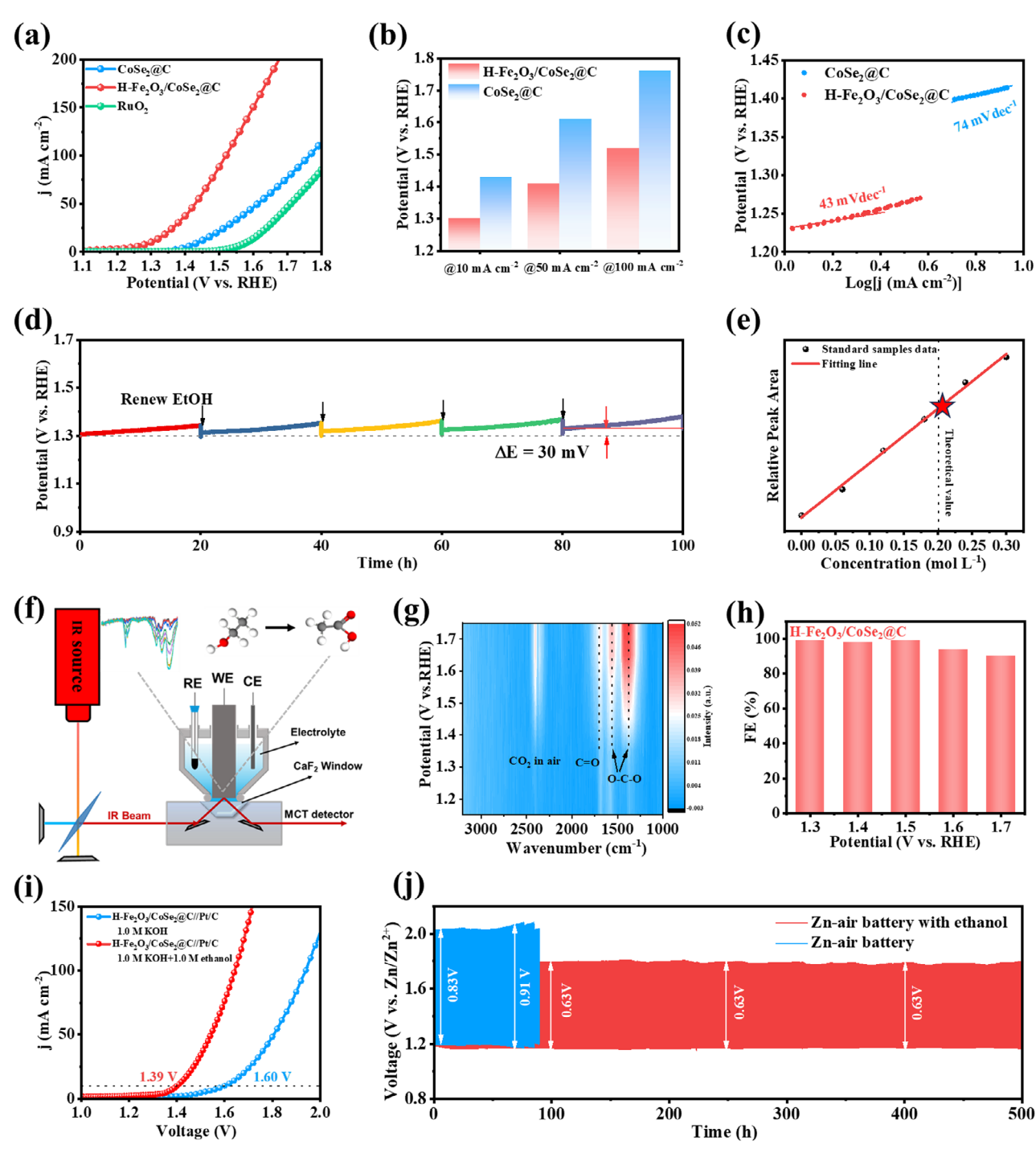


Figure 3. a) The LSVs for EOR in 1.0 M KOH solution with 1.0 M ethanol (data without iR-correction). b) The potentials of H-Fe $_2$ O $_3$ /CoSe $_2$ @C and H-CoSe $_2$ @C at 10, 50, and 100 mA cm $^{-2}$. c) The corresponding Tafel plots. d) Chronopotentiometry (CP) test of EOR at \approx 10 mA cm $^{-2}$. e) FE of EOR at 1.4 V vs. RHE. f) The model of in situ FTIR device. g) The in situ FTIR spectra of H-Fe $_2$ O $_3$ /CoSe $_2$ @C. h) FE of EOR at a different potential. i) LSVs for overall water splitting with and without ethanol. j) The long-term charge and discharge profile of Zn-air battery and ethanol-assisted Zn-air battery.

literature, the reaction pathway involves a four-electron transfer process (CH₃CH₂OH* \rightarrow CH₃CH₂O* \rightarrow CH₃CHO* \rightarrow CH₃COO*). Based on the standard curve (Figure 3e), the FE for the electro-oxidation of ethanol was quantified, the value is close to 99% at 1.30 V. To elucidate the reaction pathway, in situ FTIR

spectroscopy was conducted, as illustrated in the device setup shown in Figure 3f. The in situ FTIR spectra (Figure 3g), display peaks at 1400 and 1567 cm $^{-1}$, which are attributed to asymmetric and symmetric stretching vibrations of O—C—O in acetate, while the peaks at 1722 and 2358 cm $^{-1}$ correspond to C=O stretching

www.afm-journal.de

1616928, D. Downloaded from https://advanced.onlinelibrary.wiley.com/doi/10.1002/adfm.202599007 by National Taiwan University, Wiley Online Library on [27/10/2025], See the Terms and Conditions (https://onlinelibrary.wiley.com/terms-and-conditions) on Wiley Online Library for rules of use; O. A articles as governed by the applicable Certain Commons.

vibrations of aldehyde/ketone or acetic acid and the asymmetric vibration of CO₂. With the increasing of potential, it can be seen that the intensity of the peak of O—C—O and C=O peaks gradually intensified, which further confirms the oxidation of ethanol to acetate. Moreover, the FEs at different potentials were analyzed, as shown in Figure 3h. The H-Fe₂O₃/CoSe₂@C maintained a high FE (over 90%) for acetate formation across a wide voltage range from +1.3 to +1.7 V, which is higher than that of CoSe₂@C (Figure S19, Supporting Information), verifying that interface engineering can effectively improve the EOR activity and stability.

Building on the advantages of EOR, ethanol-assisted water electrolysis (E-WE) was evaluated for hydrogen production (Figure 3i). Compared to conventional WE, E-WE significantly reduces the cell voltage by 210 mV at 10 mA cm⁻², while simultaneously producing high-value acetic acid at the anode. Moreover, E-WE demonstrates remarkable stability, with no obvious loss in activity observed after 100 h of operation (Figure S20, Supporting Information).

Additionally, an ethanol-assisted Zn-air battery (E-ZABs) was developed (schematic in Figure S21, Supporting Information), where the ORR occurs at the air electrode during discharge, and EOR occurs during charging. As shown in Figure S22a (Supporting Information), the discharge and charge polarization curves show that the voltage gap (ΔE) between charge and discharge at 50 mA cm⁻² decreases from +1.42 to +1.22 V upon ethanol addition. The corresponding power density curves (Figure S22b, Supporting Information) indicate that H-Fe₂O₃/CoSe₂@C-based E-ZABs achieve a high-power density of 100 mW cm^{-2} at +0.87 V. The long-term charge/discharge cycling performance (Figure 3j) at 10 mA cm⁻² further demonstrates the superior stability of E-ZABs compared to conventional ZABs. In E-ZABs, the ΔE maintains stability even after 500 h cycles, whereas, in conventional ZABs, ΔE noticeably increases from the initial + 0.83 to + 0.91 V in less than 100 h. The exceptional cycling stability observed in both E-WE and E-ZABs can be attributed to two key factors: 1) EOR can significantly reduce the oxidation potential to alleviate catalyst reconstruction compared to OER; and 2) acetate formation rather than O2 prevents catalyst spalling caused by bubble formation. The above results provide a promising approach for designing efficient energy conversion systems.

In situ Raman tests were carried out to investigate the surface change during EOR, with the device schematic presented in the Figure 4a. For EOR, the appearance of broad peaks between 2900 and 3000 cm⁻¹ in in situ Raman spectra (Figure S23, Supporting Information), is attributed to the symmetric $v_s(CH)$ and asymmetric v_{as} (CH) vibrations of surface ethanol intermediate. [25] In the lower frequency range of 200-1000 cm⁻¹ (Figure 4b; Figure S24a, Supporting Information), the H-Fe₂O₃/CoSe₂@C shows a gradual decrease in CoSe₂ peaks (481 and 690 cm⁻¹) with increasing potential. A new peak at 512 cm⁻¹ emerged at +1.2 V vs. RHE, assigned to the Co-OH vibrations of Co(OH), [46] indicating the formation of Co(OH)₂. As the potential exceeds +1.5 V, the Co-OH peaks disappear, and new peaks corresponding to Co3+-O* and Co⁴⁺–O* emerge, [47] suggesting Co(OH), is further oxidized to form CoOOH species. In the absence of ethanol (Figure 4c; Figure \$24b, Supporting Information), the CoOOH species are formed at potentials more than +1.2 V, but no peaks corresponding to Co(OH)₂ can be observed. These observations suggest that

Adv. Funct. Mater. 2025, 2509007

the $CoSe_2/Fe_2O_3$ is reconstructed to form $CoOOH/Fe_2O_3$ at 1.2 V, and then CoOOH reacts with CH_3CH_2OH to form $Co(OH)_2$, suggesting the real active species for EOR are the $CoOOH/Fe_2O_3$. The detected Raman signal of $Co(OH)_2$ suggests that the EOR rate on the surface of $CoOOH/Fe_2O_3$ is faster than the oxidation rate of CoOOH in the potential range.

Furthermore, a comparison between the Raman spectrum of EOR and OER reveals that H-Fe₂O₃/CoSe₂@C undergoes more pronounced structural reconfiguration during the OER process, which further supports the notion that the substituting OER with EOR can help maintain the structural integrity of the catalyst, thereby improving its catalytic stability. To prove the effects of Fe₂O₃, the in situ Raman spectroscopy for EOR and OER of CoSe₂@C are also tested (Figure S25a,b, Supporting Information). In these spectra, the CoSe₂ gradually weakens, and Co³⁺– O* and Co4+-O* peaks emerge over +1.35 V during both EOR and OER. However, no obvious Co(OH), peaks are detected during the whole EOR process, which indicates that the EOR rate on the surface of CoOOH is slower than the oxidation rate of CoOOH during the whole range. The results confirm that the introduction of Fe₂O₃ can greatly reduce the activation potential due to the effects of push electrons, and improve the EOR catalytic activity and kinetics through electron interaction.

Furthermore, Quasi in situ XPS measurements at different potentials (detail in the experiment section) further confirm the aforementioned findings. In the Se 3d spectra (Figure S26, Supporting Information), the peaks of H-Fe₂O₃/CoSe₂@C show a gradual decrease with increasing potential, suggesting that the surface occurs during the reconstruction during EOR. In the Co2p spectra (Figure 4d,e), the absence of Co⁰ peaks in CoSe₂@C and H-Fe₂O₃/CoSe₂@C at 1.2 V vs. RHE, which further confirms that oxidation occurs on the sample surface. Figure 4f illustrates the changes in the high- and low-valent state Co species in CoSe₂@C and H-Fe₂O₃/CoSe₂@C under different reaction potentials. Generally, for CoSe₂@C, the content of high-valent state species increases with increasing potential, indicating that the Co³⁺ or Co⁴⁺ serves as the main active site at high potentials, which is advantageous for the OER process. In contrast, the H-Fe₂O₃/CoSe₂@C exhibits a decrease in the average valent state with increasing potential, as evidenced by the decreasing Co³⁺ and +Co⁴⁺ content. The content of high-valent state species begins to increase $\approx +1.6-+1.7$ V, which can provide a wide EOR window. Although the Co²⁺ content in H-Fe₂O₃/CoSe₂@C decreases at +1.6-+1.7 V vs. RHE, it is still higher than in CoSe₂@C. Concurrently, the Fe2p spectra at different potentials were also examined. Figure \$27 (Supporting Information) showed a decreasing Fe^{2+}/Fe^{3+} ratio between +1.2 and +1.6 V vs. RHE, indicating Fe²⁺ is oxidized to form Fe³⁺ with the potential increases to alleviate excessive oxidation of Co, which reflects the pulling electrons property of Fe₂O₃, thus stabling the valence state of Co³⁺ under a wide potential range. Based on the above analysis, we summarize the surface change and EOR process in H-Fe₂O₃/CoSe₂@C and CoSe₂, with corresponding schematic diagrams presented in Figures S28 and S29 (Supporting Information). The introduction of Fe₂O₃ can effectively regulate the interfacial charge of CoSe₂, accelerating reconfiguration and maintaining a stable valence state at the interface, thereby improving the EOR performance and expanding the reaction potential range.

16163028, 0, Downloaded from https://advanced.onlinelibrary.wiley.com/doi/10.1002/adfm.202509007 by National Taiwan University, Wiley Online Library on [27/10/2025]. See the Terms and Conditions (https://onlinelibrary.wiley

conditions) on Wiley Online Library for rules of use; OA articles are governed by the applicable Creative Commons

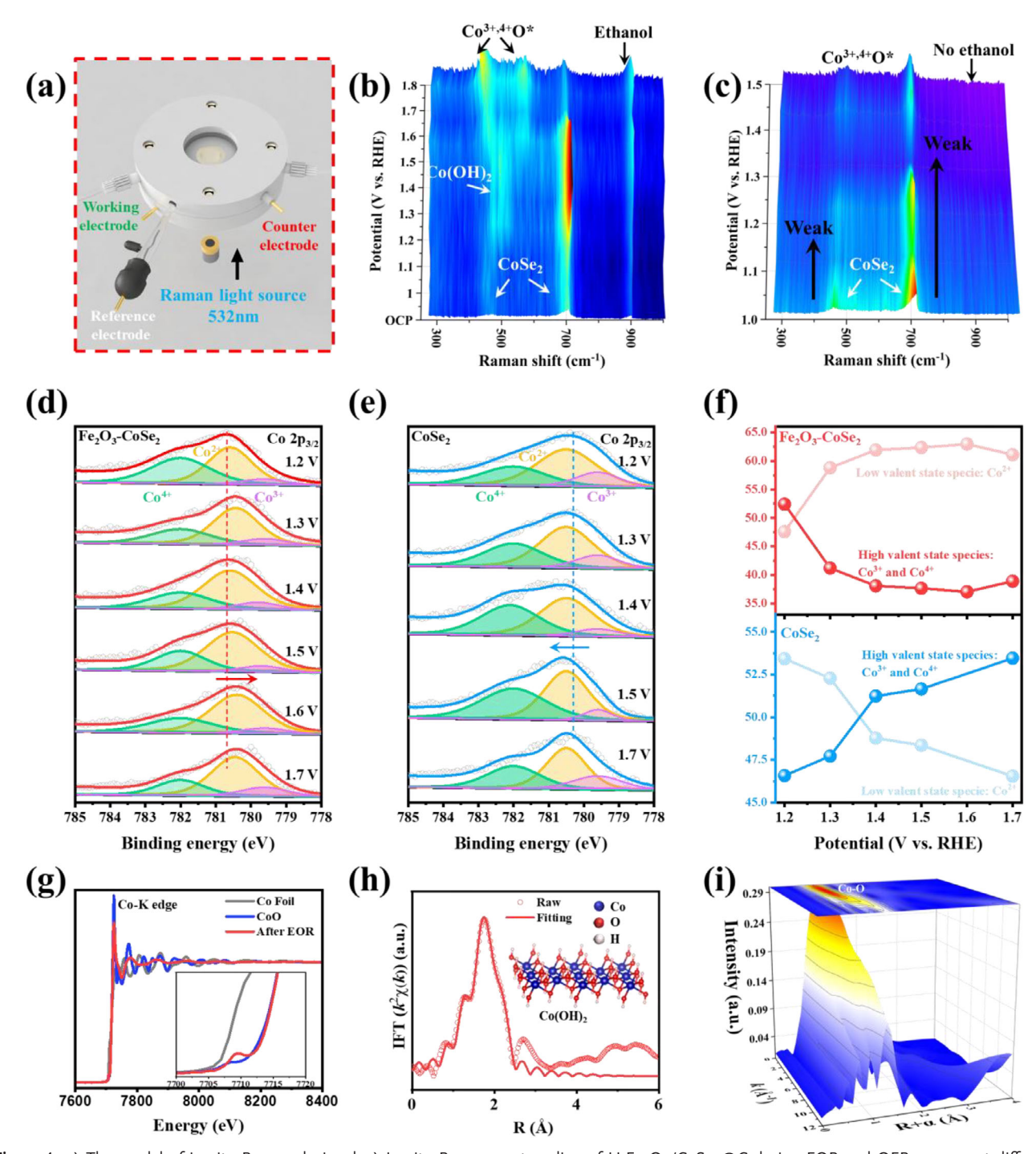


Figure 4. a) The model of in situ Raman device. b,c) In situ Raman contour line of H-Fe $_2$ O $_3$ /CoSe $_2$ @C during EOR and OER process at different potentials (vs. RHE). d,e) Quasi in situ XPS spectra of Co2p for H-Fe $_2$ O $_3$ /CoSe $_2$ @C and CoSe $_2$ @C during EOR under different potentials (vs. RHE). f) The relative contents of high/low valent state cobalt species vs. the applied potential according to the Quasi in situ XPS spectrum. g–i) The Co K adage XANES spectra, first-shell fitting spectrum, and WT profile of H-Fe $_2$ O $_3$ /CoSe $_2$ @C after EOR.

To further verify the active species, the crystalline phase, composition, and valence states after the CP tests for OER and EOR at 10 mA cm $^{-2}$ were also characterized. In TEM images after the EOR test (Figure S30a, Supporting Information), H-Fe₂O₃/CoSe₂@C still maintains its hollow structure. The corre-

sponding HRTEM images (Figure S30b–d, Supporting Information) reveal that the $CoSe_2$ phases undergo reconstruction, with clear lattice spacings of 0.23 nm corresponding to $Co(OH)_2$, which is consistent with in situ Raman spectra results. Moreover, the (222) phase of Fe_2O_3 also can be found, which

www.advancedsciencenews.com



16163028, 0. Downloaded from https://advanced.onlinelibrary.wiley.com/doi/10.1002/adfm.202599007 by National Taiwan University, Wiley Online Library on [27/10/2025], See the Terms and Conditions (https://onlinelibrary.wiley.com/terms-and-conditions) on Wiley Online Library for rules of use; O.A articles are governed by the applicable Ceravive Commons

www.afm-journal.de

suggests that Fe2O3 is stable. After the OER test, H-Fe₂O₃/CoSe₂@C also maintains a hollow structure (Figure S31a, Supporting Information), with lattice spacings of 0.44 nm corresponding to CoOOH,[49] (Figure S31b-d, Supporting Information), further confirming Raman spectra findings. To conduct a more in-depth analysis of the structural alterations in the catalyst following the long-term EOR test (lasting ≈100 h), TEM analysis was performed. As depicted in Figure S32a (Supporting Information), it can be observed that the hollow structure of the catalyst still exists after the long-term EOR test. Nevertheless, owing to the restructuring of the catalyst, certain hollow structures have transformed into a solid state. Moreover, in the corresponding mapping images (Figure S32b, Supporting Information), the elements of Co, O, C, Fe, N, and Se can still be observed. This observation indicates that the carbon species can stably exist in the sample even after the long-term EOR test.

In the O1s spectrum (Figure S33a, Supporting Information) after the EOR process, prominent Co-OH peaks at 530.9 eV suggest the formation of Co(OH)₂. The Fe2p spectrum (Figure S33b, Supporting Information) shows negligible alteration after the EOR test, indicating the stability of Fe₂O₃. The Co₂p spectra (Figure S33c, Supporting Information) reveal that only two fitting peaks at 781.5 and 796.6 eV, corresponding to Co²⁺ can be observed after long-term EOR test, further indicating that the enhanced EOR kinetics. In contrast, only Co3+peaks are observed after OER tests.[50,51] To gain further insight into the chemical state and coordination environment of H-Fe₂O₃/CoSe₂@C, XAS analysis is also conducted after the EOR test. XANES spectra (Figure 4g) of Co K-edge show that the oxidation state of Co is close to that of CoO. EXAFS spectra (Figure \$34, Supporting Information) show that the complete disappearance of Co-Se bonds and an increase in Co-O bond strength, further corroborating the oxidation of CoSe₂. The Fourier transforms of k²-weighted EXAFS fitting (Figure 4h; Table S4, Supporting Information) reveal that the Co atoms are coordinated with four O atoms and one Co atom, closely matching the theoretical value for Co(OH)₂. The WT profile (Figure 4i) shows an intensity maximum near an R space of 1.5 Å and k space of 3.0 Å⁻¹, attributing to the coordination structure of Co-O in the first coordination shell.

Subsequently, DFT calculations were used to explain the excellent performance. It is widely recognized that the chemical state plays a pivotal role in transition-metal-based catalysts, and those with higher oxidation states (+3) are more effective in alkaline EOR. Based on the above analysis, the main active structure is Fe₂O₃/CoOOH. For comparison, pure CoSe₂ and Fe₂O₃/CoSe₂ models were also constructed to study the EOR mechanism (Figure 5a). According to the Sabatier principle, [52] the interaction between the catalyst and the intermediates should have moderate adsorption-desorption energy, too strong or too weak is not suitable for the catalytic process. The d band center (E_d) serves as a useful descriptor to evaluate these interactions. Since CoOOH produced during the reaction is the main active site, it is necessary to consider both the d band center of Co and the p band center of O/Se. To further analyze the free energy band changes, the weighted energy band center of the active site is proposed: $\varepsilon_{\rm w} = [N_{\rm d}\varepsilon_{\rm d}({\rm Co}) + N_{\rm p} - \varepsilon_{\rm p} ({\rm O/Se})]/(N_{\rm d} + N_{\rm p}),$ where, $\varepsilon_d(Co)$ and $\varepsilon_p(O/Se)$ are the d and p band centers of Coand O/Se atoms, with $N_d = 10$ and $N_p = 6$, respectively. The weighted band centers of different electrocatalysts are compared,

where the $\epsilon_{\rm w}$ of Fe₂O₃/CoOOH ($\epsilon_{\rm w}=-3.14$ eV) is intermediate between that of CoSe₂ ($\epsilon_{\rm w}=-2.61$ eV) and Fe₂O₃/CoSe₂ ($\epsilon_{\rm w}=-3.41$ eV). The moderate position of the weighted d-band center for Fe₂O₃/CoOOH (Figure 5b), signifies that there exists a moderate adsorption–desorption energy between Fe₂O₃/CoOOH and the adsorbates, which suggests that the interfacial interaction within the heterojunctions may improve the adsorption of intermediates, thus increasing the EOR electrocatalytic activity.

From an energetic perspective, we calculated the energy profile for the entire catalytic process of the ethanol-to-acetic acid conversion in an alkaline medium and compared the energy cost associated with each step. The metal-site adsorbate evolution mechanism scenario, which involves proton-electron transfer steps, was considered as the reaction mechanism. As illustrated in Figure 5c, the energy required for molecular adsorption on the Co site is lower than on the Fe site. This further supports that CoOOH on Fe₂O₃/CoOOH serves as the active site in the EOR process. With the active site identified, we calculated the EOR process at the Co site of the constructed structure, including the adsorption/desorption, dehydrogenation, and hydroxyl addition of the reaction intermediates (Figure 5d). As can be seen from the free energy diagram of the EOR step in Figure 5e, the CoSe₂ presents the most challenging EOR process, with the highest energy barrier (3.02 eV) at the PDS. In contrast, the PDS for Fe₂O₃/CoOOH occurs in the final step, with Δ G of 2.22 eV, which is significantly lower than that of CoOOH (2.62 eV), thus greatly facilitating the reaction. In addition, we also calculated the energy barrier for the PDS of Fe₂O₃/CoSe₂, which, at 2.47 eV, is higher than that of Fe₂O₃/CoOOH but lower than that of CoSe₂. The DFT results further confirm that the reconstructed Fe₂O₃/CoOOH is the primary activity site for EOR, which optimizes the adsorption/desorption, dehydrogenation, and hydroxyl addition of the intermediates, resulting in superior EOR catalytic activity.

Figure 5f shows the dynamic spring electronic effect and the phase recombination differences between CoSe₂ and CoSe₂/Fe₂O₃ during ethanol oxidation. Both high valence Co³⁺ and Co⁴⁺ have catalytic oxidation activity, but Co³⁺ is more inclined toward ethanol oxidation reaction, while Co⁴⁺ mainly undergoes OER reaction. Meanwhile, OER can only be achieved through electrochemical steps on CoO₂, which results in alcohol oxidation reactions having more favorable thermodynamics and kinetics than OER. In addition, the oxidation of Co(OH)₂ can be divided into two stages, with the role of Fe₂O₃ being different in each stage, further demonstrating the dynamic spring electronic effect.

Furthermore, we have calculated the energy barrier of phase transformation from $Co(OH)_2$ to CoOOH and from CoOOH to CoO_2 , as presented in Figure 5g. After introducing Fe_2O_3 to form a heterojunction, the deprotonation energy barrier of $Co(OH)_2$ to CoOOH decreases from 1.789 to 1.336 eV. For the stage from CoOOH to CoO_2 , the energy barrier increased from 2.07 to 2.146 eV. This calculation result indicates that the introduction of Fe_2O_3 helps promote the formation of CoOOH, while also inhibiting the occurrence of CoO_2 , further verifying the dynamic electronic spring effect from a theoretical calculation perspective. To elucidate the alterations in metal valence states throughout catalytic reactions more distinctly, a mechanism involving proton-coupled electron transfer between

16163028, 0, Downloaded from https://advanced.onlinelibrary.wiley.com/doi/10.1002/adfm.202509007 by National Taiwan University, Wiley Online Library on [27/10/2025]. See the Terms and Conditions (https://on

conditions) on Wiley Online Library for rules of use; OA articles are governed by the applicable Creative Commons

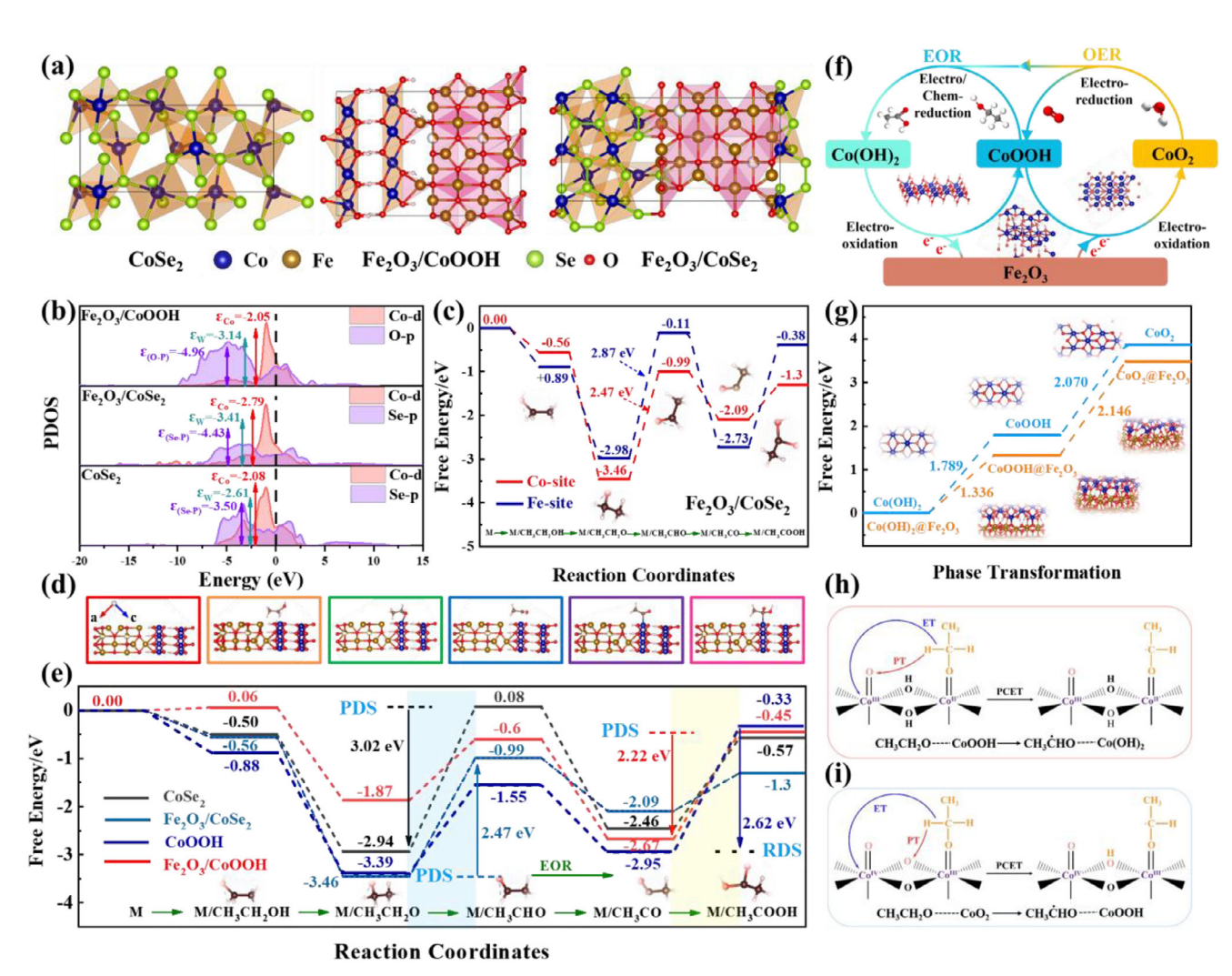


Figure 5. a) Structure representations of $CoSe_2$, $Fe_2O_3 @ CoSe_2$, and $Fe_2O_3 @ CoOOH$. b) Projected density of states (PDOS), d-band of Co, and p-band of Se/O in $CoSe_2$, $Fe_2O_3 @ CoSe_2$, and $Fe_2O_3 @ CoOOH$. c) Adsorption energy plot for ethanol conversion process at the Co and Fe sites of $Fe_2O_3 @ CoSe_2$, respectively. d) The represented adsorption models of each step of $Fe_2O_3 @ CoOOH$. e) Adsorption energy plot for ethanol conversion process of $Fe_2O_3 @ CoSe_2$, $Fe_2O_3 @ CoSe_2$ (Co site), $Fe_2O_3 @ CoOOH$ and $Fe_2O_3 @ CoOOH$ and $Fe_2O_3 @ CoOOH$ and $Fe_2O_3 @ CoOOH$ to Fe_2O_3

high-valent cobalt species and alcohols was suggested. As depicted in Figure 5h,i, the C—H bond located at the α -site of the alcohol anion that is adsorbed onto the catalysts undergoes cleavage. This process involves the transfer of a proton accompanied by an electron to the catalysts, leading to the reduction of the high-valent phase back to its original state. The oxygen groups serve as sites for proton acceptance in CoOOH and CoO2, respectively. Additionally, the alcohol anion produces carbon radicals that subsequently desorb and transform into corresponding aldehydes.

Furthermore, to elucidate the underlying reaction mechanism and the role of spin effects, we investigated the EOR process from a spintronics perspective, with more detail provided in Figure S35 and Tables S5–S9 (Supporting Information). Initially, the spin-related EOR mechanism is discussed. Generally, ethanol adsorbs onto the surface of active sites, and evolutes sequentially into ${}^{*}\text{CH}_{3}\text{CH}_{2}\text{O}$, ${}^{*}\text{CH}_{3}\text{CH}_{0}$, ${}^{*}\text{CH}_{3}\text{CO}$, and ${}^{*}\text{CH}_{3}\text{COOH}$ (Figure 6a).

During the process, the α -carbon atoms, which are linked to the hydroxy or carbonyl functional groups, act as the reaction centers for adsorption, deprotonation, and desorption. As shown in Figure 6b, the p_x , p_y , and p_z orbitals of the α -carbon atom engage in interaction with the d_{xz} , d_{yz} , and dz^2 orbitals, respectively, to form molecular orbitals. The electron occupancy within these orbitals significantly influences the spin configuration of the resultant molecular orbitals. Consequently, the electronic structures of the α -carbon atoms within the reaction intermediates play a dominant role in the overall reaction mechanism. To elucidate this further, we first calculate the electronic structures of the reaction intermediates. As depicted in Figure 6c, the occupancies of the p_x , p_y , and p_z orbitals of the α -carbon atoms vary across the intermediates analyzed. Notably, the *CH₃CH₂O intermediate exhibits an electronic structure that closely resembles that of *CH₃CH₂OH, indicating that the deprotonation of hydroxy minimally impacts the electronic configuration of the α -carbon atom.

16163028, 0, Downloaded from https://advanced

onlinelibrary.wiley.com/doi/10.1002/adfm.202509007 by National Taiwan University. Wiley Online Library on [27/10/2025]. See the Terms and Condition

conditions) on Wiley Online Library for rules of use; OA articles are governed by the applicable Creative Commons

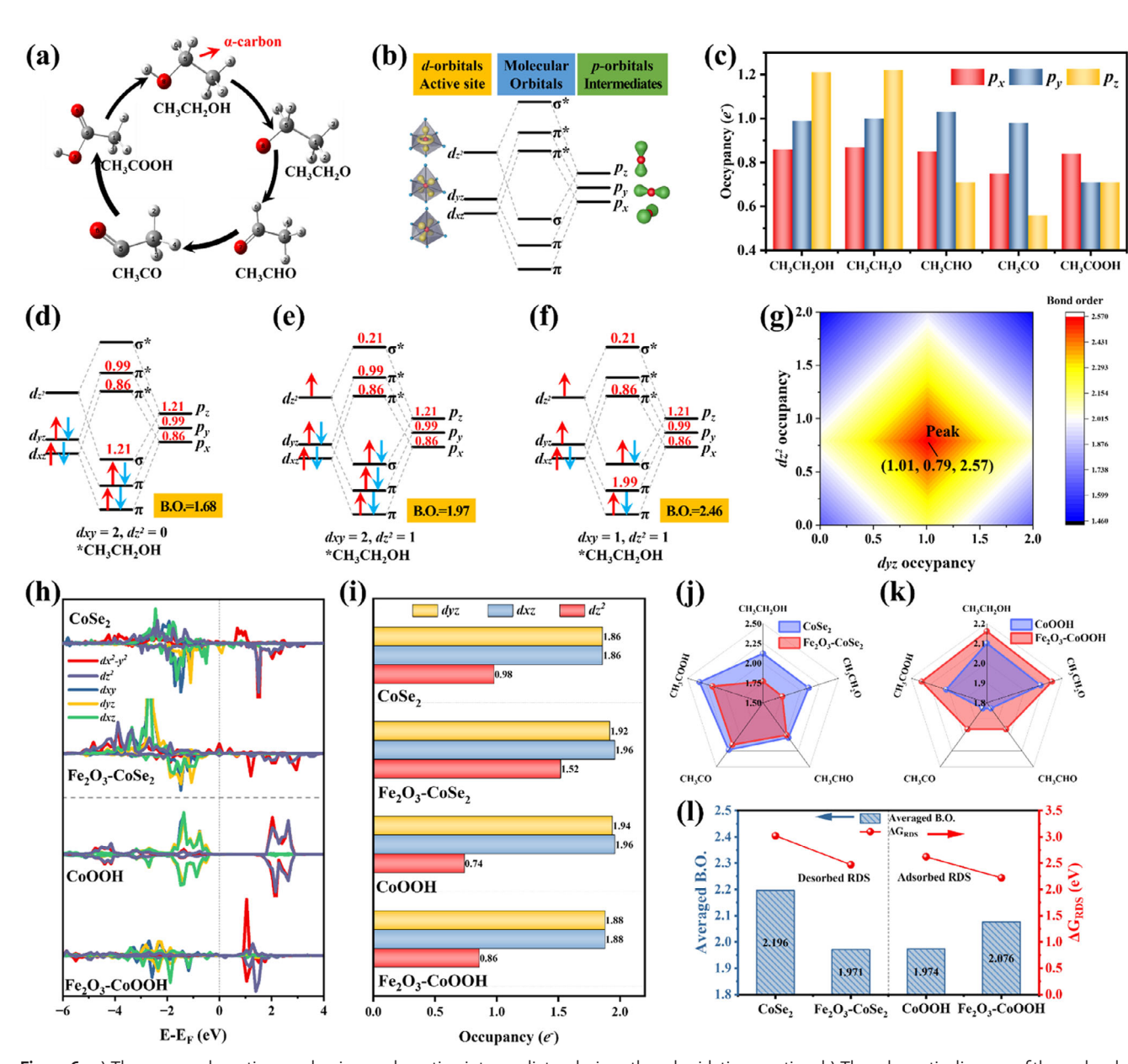


Figure 6. a) The proposed reaction mechanism and reaction intermediates during ethanol oxidation reaction. b) The schematic diagram of the molecular orbitals formation. c) The orbital occupancies of the reaction intermediates during the ethanol oxidation reaction. d–f) The bond orders between ethanol and different active sites. The bond order is calculated by $(n_{bonding}-n_{anti-bonding})/2$, where $n_{bonding}$ and $n_{anti-bonding}$ are the numbers of electrons in the bonding or anti-bonding states, respectively. g) The phase diagram of bond order between ethanol and active sites. h) The spin-resolved PDOS of the $CoSe_2$, Fe_2O_3 - $CoSe_2$, CoOOH and Fe_2O_3 -CoOOH. i) The orbital occupancies of d_{xz} , d_{yz} and dz^2 orbitals according to the PDOS. j,k) The calculated bond orders between the reaction intermediates and active sites. l) The averaged bond orders (B.O.) and the corresponding energy differences of rate-determined steps.

In contrast, the subsequent deprotonation of α -carbon atom leads to the formation of *CH $_3$ CHO and *CH $_3$ CO, resulting in a notable reduction in p_z occupancy. Finally, the adsorption of hydroxy onto CH $_3$ CO to form CH $_3$ COOH results in an increase in p_z and p_x occupancy, alongside a decline in p_y occupancy. Given the diverse electronic configurations of the intermediates, it can be anticipated that their reactivity will differ throughout the reaction. Thus, it presents a considerable challenge to simultaneously ma-

nipulate the adsorption and desorption dynamics of all intermediates involved.

Taking ethanol as an example, its orbital configuration can be expressed as $(p_x)^{0.86}(p_y)^{0.99}(p_z)^{1.21}$. The bond order (B.O.) is proposed as a metric to evaluate the strength of the bonding molecular orbits, which can reflect the ability for adsorption. A larger number of electrons occupying the bonding orbitals, coupled with a lesser number in the anti-bonding orbitals, results in a larger the B.O. and stronger adsorption potential. For transition

www.afm-journal.de

1616928, D. Downloaded from https://advanced.onlinelibrary.wiley.com/doi/10.1002/adfm.202599007 by National Taiwan University, Wiley Online Library on [27/10/2025]. See the Terms and Conditions (https://onlinelibrary.wiley.com/erms-and-conditions) on Wiley Online Library for Italian (D. 10.1002). See the Terms and Conditions (https://onlinelibrary.wiley.com/erms-and-conditions) on Wiley Online Library for Italian (D. 10.1002). The Advanced on Ita

metal atoms that exhibit electrocatalytic activity in EOR, such as Fe, Co, or Ni, it is observed that these atoms typically host more than 6 electrons in their d orbitals. Therefore, the d_{xx} orbital with the lowest orbital energy is often fully occupied, while the d_{vz} and dz^2 orbitals may contain between 0 and 2 electrons. For example, as illustrated in Figure 6d, the low-spin Co atoms present a fully occupied d_{vz} orbital and an unoccupied dz^2 orbital. When these low-spin Co atoms interact with ethanol molecules, the B.O. is calculated to be 1.68. Similarly, for the intermediate- and highspin species, the B.O for ethanol rises to 1.97 and 2.46, respectively (Figure 6e,f). This indicates that active sites with different electron configurations possess different adsorption abilities for ethanol. Furthermore, considering a more universal electron configuration where the occupancy of d_{xz} is set to 2, with the occupancies of d_{vz} and dz^2 ranging from 0 to 2, it can be found that, as shown in Figure 6g, when ethanol has a configuration of (p_y) p_z) = (0.99, 1.21, the B.O. reaches its peak with the active site configuration of $(d_{vz}, dz^2) = (1.01, 0.79)$. This indicates that ethanol forms a strong bond with high-spin species that have one unpaired electron in d_{vz} orbital and 0.79 electrons in the dz^2 orbital. Any alteration in occupancy of d_{vz} or dz^2 orbitals would weaken the adsorption of ethanol, thereby affecting the efficiency of the EOR.

Similarly, for other intermediates, when the electron configurations $(p_y, p_z)_{\text{intermediate}}$ match with $(d_{yz}, dz^2)_{\text{active site}}$ to be $(p_y, p_z)_{\text{intermediate}} + (d_{yz}, dz^2)_{\text{active site}} = (p_y + d_{yz}, p_z + dz^2) = (2, 2)$, the adsorption reaches its maximum. For instance, CH₃CHO, with an electron configuration of $(p_y, p_z) = (1.03, 0.71)$, strongly binds to active sites with electron configurations of $(d_{yz}, dz^2) = (0.97, 1.29)$, which means that CH₃CHO prefers a higher-spin site compared to CH₃CH₂OH, which has its strongest configuration at $(d_{yz}, dz^2) = (1.01, 0.79)$. In conclusion, the EOR is highly sensitive to the spin state of the active sites, as the reaction intermediates exist in various spin configurations. By matching the d orbital occupancies of active sites with the p orbital occupancies of intermediates can effectively manipulate the absorption characteristics of these intermediates

Building on the elucidation of the spin-related mechanism for the EOR, we further explore the enhanced catalytic performance. From Figure 6h, the DFT-calculated projected density of states (PDOS) reveals that the introduction of Fe₂O₃ significantly impacts the spin configuration of CoSe₂ and CoOOH. In the case of Fe₂O₃-CoSe₂, a marked reduction in the PDOS above the Fermi level is observed compared to CoSe2, indicating a higher orbital occupancy in Fe₂O₃- CoSe₂. For Fe₂O₃-CoOOH, the dyz and dxz orbitals exhibit increased PDOS, while the dz^2 orbital shows a decrease above the Fermi level compared to CoOOH, suggesting a change in the electronic structure upon Fe₂O₃ introduction. To further clarify this, orbital occupancies are calculated as shown in Figure 6i. The four catalysts under investigation exhibit nearly full configurations in the dyz and dxz orbitals. Notably, the introduction of Fe₂O₃ increases the occupancy of the dyz and dxz orbitals in CoSe₂. Conversely, it results in a decrease in the occupancy of these orbitals in CoOOH. Additionally, both Fe₂O₃-CoSe₂ and Fe₂O₃-CoOOH show an increase in electron occupancy within the dz^2 orbital. Given these distinct spin configurations, the active sites are expected to exhibit varying abilities to adsorb reaction intermediates. As shown in Figure 6j,k, Fe₂O₃-CoSe₂ demonstrates lower B.O. for all intermediates compared to CoSe2, indicating a reduced adsorption capacity. In contrast, Fe₂O₃-CoOOH shows a higher adsorption ability for all studied intermediates compared to CoOOH. The contrasting effects of Fe₂O₃ on CoSe₂ and CoOOH further emphasize the 'spring' effect of Fe₂O₃ and can be explained as follows. In light of the foregoing analysis, the PDS for CoSe2 and Fe2O3-CoSe2 is the deprotonation process, which is a desorption step. The introduction of Fe₂O₃ weakens the adsorption ability of CoSe₂, facilitating the desorption of the PDS. This result aligns with the widely accepted d-band theory, which suggests that Fe₂O₃-CoSe₂ features a lower d-band center. Conversely, the PDS for CoOOH and Fe $_2\text{O}_3\text{--}$ CoOOH involves the adsorption of hydroxyl groups, which is the adsorption step. Therefore, the enhanced adsorption ability after introducing Fe₂O₃ accelerates the adsorption of the PDS. In summary, Fe₂O₃'s role as an electronic modifier induces the 'spring' effect, where its presence adjusts the adsorption capacities of CoSe₂ and CoOOH in opposite directions. This finely tuned modification optimizes the adsorption of all intermediates, balancing the strengths and weaknesses of each catalyst to achieve enhanced OER performance. By strategically introducing Fe₂O₃, the spin configurations of CoSe₂ and CoOOH are adjusted in a way that amplifies their catalytic activity, effectively highlighting the spring effect as a key factor in optimizing catalytic processes.

3. Conclusion

In summary, H-Fe₂O₃/CoSe₂@C was synthesized through interface engineering, demonstrating exceptional electrocatalytic performance for the EOR. In situ FTIR, in situ Raman, XPS spectra, and DFT analyses reveal that Fe₂O₃ modulates the electronic and spin states of Co sites, promoting the rapid formation of Fe₂O₃/CoOOH heterostructure while inhibiting CoO₂ evolution. This regulation lowers the energy barrier of the PDS, enhances EOR kinetics, and stabilizes Co3+ across a wide potential range (1.2–1.7 V vs. RHE), achieving a Faradaic efficiency above 90%. Consequently, H-Fe₂O₃/CoSe₂@C exhibits high activity (j of 10 mA cm⁻² at 1.30 V vs. RHE), remarkable selectivity (FE over 90% between 1.2 and 1.7 V) and maintains stability over 100 h. The energy conversion efficiency and stability of based on ethanol-assisted water electrolysis and Zn-air battery have been significantly improved. This work provides valuable guidance for designing heterostructured electrocatalysts with high performance and advancing the development of hybrid energy systems.

4. Experimental Section

Preparation of ZIF-67: ZIF-67 nanoparticles (NPs) were synthesized following a previously reported method. [54] Briefly, 1.0 mmol of Co(NO)₃ was dissolved in 25 mL of methanol to form solution A. Separately, 8.0 mmol of 2-dimethylimidazole (2-MIM) was dissolved in 25 mL of methanol to prepare solution B. Then, solution B was rapidly added to solution A under constant stirring at room temperature for 20 min. The resulting mixture was aged for 24 h. After aging, he ZIF-67 NPs were washed with ethanol 3 times and collected by centrifugation.

Preparation of ZIF-67@PBA: To synthesize ZIF-67@PBA, 44 mg of as-prepared ZIF-67 was dispersed in 30 mL of ethanol using ultrasound for 30 min. Subsequently, 5 mL of an aqueous solution containing 50 mg $\rm K_3[Fe(CN)]_6$ was added dropwise to the suspension and stirred for at least 2 h. The product was then washed with deionized water (DIW) and ethanol, followed by dry in an oven at 60 °C for 12 h.

ADVANCED
FUNCTIONAL
MATERIALS

rent density of 10 mA $\rm cm^{-2},$ and the charging and discharging time was 10 min.

Assisted-water electrolysis measurements were performed by a CHI660E electrochemical workstation using a two-electrode system. The LSV was recorded over a potential range of 1.0–2.0 V vs. RHE at a scan rate of 10 mV s $^{-1}$ in a 1.0 m KOH solution containing 1.0 m ethanol. The stability of the system was evaluated by chronoamperometry at a current density of 10 mA cm $^{-2}$.

DFT Analysis: Density functional theory (DFT) calculations were performed in the castep code of Material Studio R17.2. The generalized gradient approximation (GGA) and the Perdew–Burke–Ernzerhof (PBE) function was used to describe exchange-correlation energy. The k-point mesh and cutoff energy for plane-wave expansions were set to "3 \times 1 \times 1" and 571.4 eV, respectively.

The atomic positions were relaxed until the force on each atom was less than 0.03 eV Å $^{-1}$ and the convergence tolerance of the energy was set to 10^{-5} eV. To eliminate interplanar interactions, the vacuum space of 15 Å was applied to each slab model. The (110) surface of Fe $_2$ O $_3$ and (211) surface of CoSe $_2$ were selected as the optimal exposed surfaces for constructing the Fe $_2$ O $_3$ @CoSe $_2$ heterostructure, with a lattice mismatch of less than 5%. For geometry optimization of all slab models, the top layers were allowed to relax and the bottom layers were fixed during optimization. The adsorption energy (Δ E) was calculated by the formula as follows:

$$\Delta E = E_{adsorbate+slab} - E_{adsorbate} - E_{slab}$$
 (1)

where $E_{adsorbate+slab}$, $E_{adsorbate}$, and E_{slab} represent the total energy of the adsorbate binding with the slab, the energy of the adsorbate in the gas phase and the bare slab, respectively. The Gibbs free energy change (ΔG) of an elementary reaction was estimated by $\Delta G = \Delta E + \Delta ZPE - T\Delta S$.

Supporting Information

Supporting Information is available from the Wiley Online Library or from the author.

Acknowledgements

This work was supported by the National Natural Science Foundation of China (22209056), the Guangdong Basic and Applied Basic Research Foundation (2023A1515010921, 2023A1515010270); the Postdoctoral Research Foundation of China (2020M673071) and the Science and Technology Planning Project of Guangzhou, China (Grant No. 201605030008, 202102020963), the Key Research & Development and Promotion Projects in Henan Province (242102241033).

Conflict of Interest

The authors declare no conflict of interest.

Data Availability Statement

The data that support the findings of this study are available from the corresponding author upon reasonable request.

Keywords

electronic structure regulation, ethanol oxidation reaction, Fe₂O₃/CoSe₂ heterostructure, spring effect

Received: April 9, 2025 Revised: May 18, 2025 Published online:

Preparation of $H\text{-}Fe_2O_3/CoSe_2@C$: For the synthesis of $H\text{-}Fe_2O_3/CoSe_2@C$, 100 mg of as-prepared ZIF-67@PBA was dispersed in 40 mL of ethanol by ultrasound for 30 min. Then, 30 mL of DIW containing 50 mg SeO_2 was added to the above suspension, and the mixture was stirred for 1h. The precipitates ($CoSeO_3@PBA$) were collected by filtration and dried. The dried $SeO_3@PBA$ was then placed in a tubular furnace and annealed at different temperatures for 2h under a nitrogen (N_2) gas atmosphere to form $H\text{-}Fe_2O_3/CoSe_2@C$.

For comparison, $CoSe_2@C$ was synthesized using the same procedure but without adding $K_3[Fe(CN)]_6$. 100 mg of as-prepared ZIF-67 was dispersed in 40 mL of ethanol by ultrasound for 30 min, and then adding 30 mL SeO_2 solution under stirring for 1h. The precipitates ($CoSeO_3@PBA$) were collected by filtration and dried. Finally, the $CoSe_2@C$ was obtained by annealing 2h at N_2 atmosphere.

Materials Characterization: The morphologies and structure of asmade samples were observed by field emission scanning electron microscope (FESEM, Hitachi S-4800) and transmission electron microscopy (TEM, JEOL JEM-2100). The information of crystalline phases was analyzed by X-ray diffraction (XRD, Mniflex600). The surface chemical composition and oxidation state of as-fabricated materials were analyzed by X-ray photoelectron spectroscopy (XPS). Surface area and corresponding pore structure are assessed by BET analysis (ASAP 2010 instrument) with the Barrett–Joyner–Halenda (BJH) method. X-ray absorption spectroscopy (XAS) (Beijing Synchrotron Radiation Facility) was used to analyze the coordination environment and structure of Co atoms. In situ Raman measurement (Zolix RTS-Mini) was performed to analyze the change of surface structure, with laser wavelength at 532 nm. In situ Fourier transform infrared reflection (FTIR) spectroscopy and Nuclear Magnetic Resonance Spectroscopy (1HNMR, Bruker Ascend 600M) was performed to analyze the products.

Quasi in situ X-ray photoelectron spectroscopy (XPS) characterization: Quasi in situ XPS measurements were performed using a Thermofisher Scientific ESCALAB Xi+ instrument with a monochromatic Al K α X-ray source (1486.6 eV) operating at 15 kV and 150 W under ultra-high vacuum (7 \times 10 $^{-9}$ Pa). The total energy resolution was 0.10 eV. The fabrication method of the working electrode is consistent with the electrochemical measurement Before collecting XPS data, a sealed 1 m KOH cell equipped with a platinum counterelectrode and a Hg/HgO reference electrode was saturated with N $_2$. The working electrode was first held at each potential (OCP, 1.2, 1.3, 1.4, 1.5, and 1.6 V vs RHE) for 10 min, then the working electrode was vacuumed in the preparation chamber and finally transferred to the test chamber for XPS spectrum collection without being exposed to air. All spectra were processed using the Shirley background correction, and calibrated with the C 1s component at 284.8 eV. The Gaussian–Lorentzian line shape was adopted to fit the spectra.

Electrochemical Measurements: Electrochemical measurements were carried out by a standard three-electrode system. The working electrode was catalyst-modified carbon cloth (area: 0.25 cm⁻², loading: 0.5 mg cm⁻²). A graphite rod served as the counter electrode, and Ag/AgCl electrode was used as a reference electrode. The linear sweep voltammetry (LSV) without iR-correction for EOR was performed in a potential range of 1.0-2.0 V vs. RHE, with a scan rate of 10 mV s^{-1} in 1.0 M KOH solution containing 1.0 M ethanol. The electrochemical impedance spectroscopy (EIS) was employed to evaluate the charge transfer impedance (Rct) by performing AC impedance measurement at a potential of 1.38 V vs. RHE, over a the frequency range from 0.01 to 100 000 Hz. The electrochemical double layer capacity (C_{dl}) was determined by cyclic voltammetry (CV)within the non-Faraday region (1.0-1.1 V vs. RHE) at different scan rates (40, 80, 120, 160 and 200 mV s⁻¹). The stability of H-Fe₂O₃/CoSe₂@C was assessed by chronopotentiometry (CP) at a constant potential of 1.45 V vs. RHE.

Ethanol Assisted Zn-Air Battery/Water Electrolysis Measurements: The ethanol-assisted Zn-air battery test was conducted by a LANHE CT2001A instrument. A home-made ethanol-assisted Zn-air battery was assembled with a catalyst-modified carbon cloth (area: 1.0 cm⁻², loading: 1.0 mg cm⁻²) as the air electrode, a Zn plate as anode and an aqueous electrolyte solution containing 5 m KOH, 1m ethanol, and 0.2 m Zn(Ac). Long-term charge and discharge tests were performed at a cur-

ADVANCED
FUNCTIONAL
MATERIALS

16163028, 0, Downloaded from https://advanced.onlinelibrary.wiley.com/doi/10.1002/adfm.202509007 by National Taiwan University, Wiley Online Library on [27/10/2025]. See the Terms and Conditions (https://onlinelibrary.wiley.

conditions) on Wiley Online Library for rules of use; OA

are governed by the applicable Creative Commons

- [1] K. Miao, W. Jiang, Z. Chen, Y. Luo, D. Xiang, C. Wang, X. Kang, Adv. Mater. 2024, 36, 2308490.
- [2] H.-F. Wang, L. Chen, H. Pang, S. Kaskel, Q. Xu, Chem. Soc. Rev. 2020, 49, 1414.
- [3] Y.-P. Deng, Y. Jiang, R. Liang, N. Chen, W. Chen, Z.-W. Yin, G. King, D. Su, X. Wang, Z. Chen, J. Am. Chem. Soc. 2023, 145, 20248.
- [4] W. Wang, Y.-B. Zhu, Q. Wen, Y. Wang, J. Xia, C. Li, M.-W. Chen, Y. Liu, H. Li, H.-A. Wu, T. Zhai, Adv. Mater. 2019, 31, 1900528.
- [5] T. Wang, X. Cao, L. Jiao, Angew. Chem. Int. Ed. 2022, 61, 202213328.
- [6] J.-T. Ren, L. Chen, H.-Y. Wang, W.-W. Tian, Z.-Y. Yuan, Energy Environ. Sci. 2024, 17, 49.
- [7] H. Cheng, B. Dong, Q. Liu, F. Wang, J. Am. Chem. Soc. 2023, 145, 26858.
- [8] Z. Li, S. Ning, J. Xu, J. Zhu, Z. Yuan, Y. Wu, J. Chen, F. Xie, Y. Jin, N. Wang, H. Meng, S. Sun, Energy Environ. Sci. 2022, 15, 5300.
- [9] Z. Li, S. Ning, Y. Jin, N. Wang, S. Sun, H. Meng, Energy Environ. Sci. 2025, 18, 1002.
- [10] H. Luo, J. Barrio, N. Sunny, A. Li, L. Steier, N. Shah, I. E. L. Stephens, M.-M. Titirici, Adv. Energy Mater. 2021, 11, 2101180.
- [11] G. Chen, X. Li, X. Feng, Angew. Chem. Int. Ed. 2022, 61, 202209014.
- [12] X. Xu, X. Wang, S. Huo, X. Liu, X. Ma, M. Liu, J. Zou, Adv. Mater. 2024, 36, 2306844.
- [13] Y. Ye, J. Xu, X. Li, Y. Jian, F. Xie, J. Chen, Y. Jin, X. Yu, M.-H. Lee, N. Wang, S. Sun, H. Meng, Adv. Mater. 2024, 36, 2312618.
- [14] R. Zhang, Z. Wei, G. Ye, G. Chen, J. Miao, X. Zhou, X. Zhu, X. Cao, X. Sun, Adv. Energy Mater. 2021, 11, 2101758.
- [15] M. Luo, W. Sun, B. B. Xu, H. Pan, Y. Jiang, Adv. Energy Mater. 2021, 11, 2002762.
- [16] X. Zhao, M. Liu, Y. Wang, Y. Xiong, P. Yang, J. Qin, X. Xiong, Y. Lei, ACS Nano. 2022, 16, 19959.
- [17] T.-G. Vo, G.-S. Tran, C.-L. Chiang, Y.-G. Lin, H.-E. Chang, H.-H. Kuo, C.-Y. Chiang, Y.-J. Hsu, Adv. Funct. Mater. 2023, 33, 2209386.
- [18] W. Wan, S. C. Ammal, Z. Lin, K.-E. You, A. Heyden, J. G. Chen, Nat. Commun. 2018, 9, 4612.
- [19] D. Zhao, G.-Q. Yu, J. Xu, Q. Wu, W. Zhou, S. Ning, X.-B. Li, L. Li, N. Wang, Energy Storage Mater. 2024, 66, 103236.
- [20] X. Liu, K. Ni, B. Wen, R. Guo, C. Niu, J. Meng, Q. Li, P. Wu, Y. Zhu, X. Wu, L. Mai, ACS Energy Lett. 2019, 4, 2585.
- [21] Y. Zhao, X. F. Lu, G. Fan, D. Luan, X. Gu, X. W. Lou, *Angew. Chem. Int.*
- Ed. **2022**, 61, 202212542. [22] J. Liu, X. Meng, J. Xie, B. Liu, B. Tang, R. Wang, C. Wang, P. Gu, Y.
- Song, S. Huo, J. Zou, Adv. Funct. Mater. 2023, 33, 2300579.
 [23] R. Wang, J. Liu, J. Xie, Z. Cai, Y. Yu, Z. Zhang, X. Meng, C. Wang, X. Xu, J. Zou, Appl Catal B: Environ 2023, 324, 122230.
- Z. Zhang, Z. Zhang, X. Chen, H. Wang, H. Lu, Z. Shi, S. Feng, CCS Chemistry 2024, 6, 1324.
- [25] B. Zhao, J. Liu, C. Xu, R. Feng, P. Sui, L. Wang, J. Zhang, J.-L. Luo, X.-Z. Fu, Adv. Funct. Mater. 2021, 31, 2008812.
- [26] W. Chen, C. Xie, Y. Wang, Y. Zou, C.-L. Dong, Y.-C. Huang, Z. Xiao, Z. Wei, S. Du, C. Chen, B. Zhou, J. Ma, S. Wang, Chem 2020, 6, 2974.
- [27] Y.-Q. Zhu, H. Zhou, J. Dong, S.-M. Xu, M. Xu, L. Zheng, Q. Xu, L. Ma, Z. Li, M. Shao, H. Duan, Angew. Chem. Int. Ed. 2023, 62, 202219048.
- [28] K. A. Persson, B. Waldwick, P. Lazic, G. Ceder, Phys. Rev. B 2012, 85, 235438.

- [29] A. M. Patel, J. K. Nørskov, K. A. Persson, J. H. Montoya, *Phys. Chem. Chem. Phys.* 2019, 21, 25323.
- [30] A. Jain, S. P. Ong, G. Hautier, W. Chen, W. D. Richards, S. Dacek, S. Cholia, D. Gunter, D. Skinner, G. Ceder, K. A. Persson, APL Mater. 2013, 1, 011002.
- [31] X. Wang, L. Yu, B. Y. Guan, S. Song, X. W. Lou, Adv. Mater. 2018, 30, 1801211.
- [32] H. Zhang, A. Chen, Z. Bi, X. Wang, X. Liu, Q. Kong, W. Zhang, L. Mai, G. Hu, ACS Nano 2023, 17, 24070.
- [33] Y. Fang, X.-Y. Yu, X. W. Lou, Adv. Mater. 2018, 30, 1706668.
- [34] J. Yang, H. Gao, S. Men, Z. Shi, Z. Lin, X. Kang, S. Chen, Adv. Sci. 2018, 5, 1800763.
- [35] S. Xin, Y. Tang, B. Jia, Z. Zhang, C. Li, R. Bao, C. Li, J. Yi, J. Wang, T. Ma, Adv. Funct. Mater. 2023, 33, 2305243.
- [36] S. H. Lee, J. Kim, D. Y. Chung, J. M. Yoo, H. S. Lee, M. J. Kim, B. S. Mun, S. G. Kwon, Y.-E. Sung, T. Hyeon, J. Am. Chem. Soc. 2019, 141, 2035.
- [37] Y. Sun, X. Li, T. Zhang, K. Xu, Y. Yang, G. Chen, C. Li, Y. Xie, Angew. Chem. Int. Ed. 2021, 60, 21575.
- [38] N. Xi, Y. Zang, X. Sun, J. Yu, M. Johnsson, Y. Dai, Y. Sang, H. Liu, X. Yu, Adv. Energy Mater. 2023, 13, 2301572.
- [39] M. Yousaf, Y. Chen, H. Tabassum, Z. Wang, Y. Wang, A. Y. Abid, A. Mahmood, N. Mahmood, S. Guo, R. P. S. Han, P. Gao, Adv. Sci. 2020, 7. 1902907.
- [40] J. Dai, D. Zhao, W. Sun, X. Zhu, L. Ma, Z. Wu, C. Yang, Z. Cui, L. Li, S. Chen, ACS Catal. 2019, 9, 10761.
- [41] J. Wang, R. Gao, L. Zheng, Z. Chen, Z. Wu, L. Sun, Z. Hu, X. Liu, ACS Catal. 2018, 8, 8953.
- [42] C. Jiang, J. Yang, T. Zhao, L. Xiong, J. Tang, Appl Catal B: Environ 2021, 282, 119571.
- [43] H.-J. Liu, S. Zhang, W.-Y. Yang, N. Yu, C.-Y. Liu, Y.-M. Chai, B. Dong, Adv. Funct. Mater. 2023, 33, 2303776.
- [44] H. Zhang, T. Wang, A. Sumboja, W. Zang, J. Xie, D. Gao, S. J. Pennycook, Z. Liu, C. Guan, J. Wang, Adv. Funct. Mater. 2018, 28, 1804846.
- [45] X. Zhao, X. Yulin, Z. Liangyong, L. Sicheng, A. Fawad, Z. Jie, J. Catal. 2018, 368, 155
- [46] P. Gao, Y. Zeng, P. Tang, Z. Wang, J. Yang, A. Hu, J. Liu, Adv. Funct. Mater. 2022, 32, 2108644.
- [47] H. Jia, N. Yao, C. Yu, H. Cong, W. Luo, Angew. Chem. Int. Ed. 2023, 62, 202313886.
- [48] Q. Zhang, W. Xiao, W. H. Guo, Y. X. Yang, J. L. Lei, H. Q. Luo, N. B. Li. Adv. Funct. Mater. 2021. 31, 2102117.
- [49] S. Song, H. Bao, X. Lin, X.-L. Du, J. Zhou, L. Zhang, N. Chen, J. Hu, J.-Q. Wang, J. Energy Chem. 2020, 42, 5.
- [50] K. L. Zhou, C. Wang, Z. Wang, C. B. Han, Q. Zhang, X. Ke, J. Liu, H. Wang, Energy Environ. Sci. 2020, 13, 3082.
- [51] S. Ye, J. Wang, J. Hu, Z. Chen, L. Zheng, Y. Fu, Y. Lei, X. Ren, C. He, Q. Zhang, J. Liu, ACS Catal. 2021, 11, 6104.
- [52] J. Tian, Y. Rao, W. Shi, J. Yang, W. Ning, H. Li, Y. Yao, H. Zhou, S. Guo, Angew Chem Int Ed 2023, 62, 202310894.
- [53] B. Zhu, B. Dong, F. Wang, Q. Yang, Y. He, C. Zhang, P. Jin, L. Feng, Nat. Commun. 2023, 14, 1686.
- [54] S. Liu, Z. Wang, S. Zhou, F. Yu, M. Yu, C.-Y. Chiang, W. Zhou, J. Zhao, J. Qiu, Adv. Mater. 2017, 29, 1700874.